

# The Structure of the Stellar Disks of Southern S0 Galaxies in Sparse Environments

O. K. Sil'chenko<sup>1\*</sup>, A. Yu. Kniazev<sup>1,2,3</sup>, and E. M. Chudakova<sup>1</sup>

<sup>1</sup>*Sternberg Astronomical Institute, Lomonosov Moscow State University, Moscow, Russia*

<sup>2</sup>*South African Astronomical Observatory, P.O. Box 9, Observatory, 7935, South Africa*

<sup>3</sup>*Southern African Large Telescope, Old Frasersburg Road, Sutherland, 6920, South Africa*

Received February 24, 2015; in final form, June 26, 2015

**Abstract**—Surface photometry data are presented for 12 southern lenticular galaxies located in regions of low density. Digital images in the *gri* bands were obtained on the LCOGT network of meter-class telescopes. Structural parameters of the global stellar disks of the galaxies are calculated—the exponential scale and relative thickness. The presence of substructure in the disks is noted; in particular, more than half the studied galaxies possess ring structures, sometimes more than one. The color maps presented indicate complex evolution of the substructure of the disks of lenticular galaxies: they can be classified as blue (ongoing star formation) or red (concentration of dust). The rings do not always lie in the main plane of the disk; there are cases of clearly inclined, or even polar, compact rings.

**DOI:** 10.1134/S1063772915120057

## 1. INTRODUCTION

The structure of disk galaxies has been a subject of study over the last 50 years, first using crude photographic surface photometry and later becoming more detailed and accurate with the transition to digital detectors, with more and more substructure being identified with time. However, the patterns shown by this structure are not fully clear. Early on, it seemed fully satisfactory (and even physically, dynamically, and evolutionarily well justified) to divide any disk galaxy into two standard components—a spherical bulge with a de Vaucouleur's surface-brightness profile and a flat disk with an exponential brightness profile [1]. However, with the appearance of deep, accurate CCD photometry, multiple types of bulge brightness profiles began to appear; in many galaxies, these suddenly switched to exponential [2, 3]. Further, multi-tiered structures such as superpositions of exponentials with various scales were discovered in some disks as well.

Erwin et al. [4, 5] and Pohlen and Trujillo [6] proposed to classify the brightness profiles of disks according to three types: purely exponential, with a single scale over the entire extent of the disk; truncated, with piecewise exponential sections with a smaller outer scale; and anti-truncated, with a larger outer scale. The form of the surface-brightness profile of a disk probably reflects its secular dynamical evolution,

but there is no unified opinion about the mechanisms giving rise to particular types of profiles. For example, anti-truncated surface-brightness profiles can be obtained as a result of the accretion of a small, gasless companion [7], or as a result of a so-called major merger with an appreciable amount of gas [8]. A purely exponential disk can be interpreted as a result of the initial distribution of the gas in the volume of the dark halo and in time (see, e.g., [9]), or as the result of viscous losses of angular momentum and the radial redistribution of the gas in the disk in the process of star formation on time scales of the order of a billion years [10, 11]. It may be possible to diagnose these dynamical processes by comparing the shape of the radial surface-brightness profile of a disk with its geometrical thickness, which is very sensitive to dynamical heating as a result of viscous mergers. Our first results in this area suggested that there stable differences in the thicknesses of stellar disks with different surface-brightness profiles can exist [12].

Recent studies have suggested that the density of the galactic environment can also influence the brightness profile of the disk. An absence of S0 galaxies with truncated disks in clusters was found in [13], based on a comparison of the disk structures of S0 galaxies in Virgo and of S0 field galaxies, and in [14], based on Hubble Space Telescope data for galaxies of the distant cluster Abell 901/2 and the surrounding field. In contrast, such galaxies make up at least a quarter of all S0 galaxies in the field [15]. Thus, the

\*E-mail: sil@sai.msu.su

**Table 1.** Global parameters of the studied galaxies

Galaxy	Type (NED*)	$R_{25}$ (RC3**)	$V_r$ , km/s (NED)	Distance, Mpc (NED)	$B_T^0$ (RC3)	$M_B$ (RC3 + NED)	$\Delta$ , Mpc***	$\Delta m_B^{****}$
ESO 058-G019	SAB0-	50''	4247	55	13.57	-20.1	0.10	2.52
ESO 420-G013	SA0+(r) pec?	30	3570	47	13.52	-19.8	0.59	4.8
ESO 423-G024	SA0 <sup>0</sup> ? pec	53	3940	51.6	13.06	-20.5	0.70	0.4
IC 1608	(R)SA0+(r) pec?	61	3463	47	13.61	-19.75	0.031	5.2
NGC 216	S0 <sup>0</sup> ? edge-on	61	1544	21.4	13.57	-18.1	0.04	1.5
NGC 1210	(R')SB0+(rs) pec	60	3878	52	13.50	-20.1	0.51	2.34
NGC 1930	SAB0+(s):	56	4339	57	13.20	-20.6	0.27	1.24
NGC 2267	SB0 <sup>0</sup> (r)	50	1545	18	13.23	-18.1	0.63	2.83
NGC 2310	S0 edge-on	131	1142	13	12.11	-18.4	0.45	0.0
NGC 6893	SAB(s)0 <sup>0</sup>	77	3056	41.5	12.47	-20.6	0.58	2.8
NGC 7702	(R)SA0+(r)	66	3231	43	13.03	-20.15	0.2?	7?
NGC 7744	SAB0-(s)	66	3098	42	12.61	-20.5	-	-

\* NASA/IPAC Extragalactic Database.

\*\* Third Reference Catalog of Bright Galaxies [19].

\*\*\* Distance to nearest neighbor (NED).

\*\*\*\* Magnitude difference for nearest neighbor (NED).

environment apparently influences the outer structure of galactic disks, through either gravitational, tidal interactions or the gas-dynamical pressure of the hot intergalactic medium.

Studying lenticular galaxies as representatives of the class of disk galaxies has some advantages. The disk structures of S0 galaxies do not differ fundamentally from those of spiral galaxies [16]. At the same time, the stellar population of S0 disks is old and more uniform than the stellar populations of spiral galaxies, which facilitates morphological studies. The disks of S0 galaxies probably formed in fairly rapid star-forming events, as is suggested by the high ratio of magnesium to iron in their stellar populations [17, 18], and this already substantially constrains scenarios for the formation of exponential brightness (density) profiles, since it excludes very long time scales.

We begin our study of the disk structures of S0 galaxies with a small sample of Southern objects located in regions of low density. The LCOGT network of meter-class telescopes was used to obtain CCD images of 12 S0 galaxies in three filters, whose radial and vertical structures were analyzed. The global characteristics of the galaxies collected from the literature are presented in Table 1. The galaxies were chosen to be in fairly sparse environments, and none are members of clusters or rich groups. In addition

to the morphological types, sizes, and luminosities of the galaxies, Table 1 gives information about the nearest neighbors, which were selected from the NED database using the ‘‘Submit Environment Search’’ facility, which takes into account not only the distance between the objects in the plane of the sky, but also the closeness of their radial velocities.

## 2. OBSERVATIONS AND PRIMARY REDUCTION

The observations were carried out in the service regime of the Las Cumbres Observatory Global Telescope (LCOGT). By May 2013, the LCOGT consisted of two 2-m optical telescopes, dozens of 1-m telescopes, and one 83-cm telescope located at six observatories, three in the Northern and three in the Southern hemisphere. This makes it possible to carry out photometric and spectral observations of objects regardless of their declinations, create continuous time series of observations, operatively acquire spectra of recently discovered supernovae, and much more [20]. It is planned to increase the number of meter-class telescopes to 15 in the near future. During our observations, all the LCOGT meter-class telescopes were outfitted with standard SBIG cameras for the acquisition of direct frames. This camera consists of a 4000 × 4000 Kodak KAF-16803 CCD. With the physical pixel size of this CCD, 9  $\mu\text{m}$ , and standard

**Table 2.** Journal of observations

Galaxy	Telescope	Date	Filter	Exposure, s	FWHM
1	2	3	4	5	6
ESO 058-G019	Cerro Tololo, 1m0-04	30.11.2013	<i>g</i>	450 × 4	2.0''
ESO 058-G019	Cerro Tololo, 1m0-04	30.11.2013	<i>i</i>	600 × 2	2.0
ESO 058-G019	Cerro Tololo, 1m0-04	30.11.2013	<i>r</i>	600 × 2	2.0
ESO 420-G013	Cerro Tololo, 1m0-05	29.11.2013	<i>g</i>	450 × 4	1.8
ESO 420-G013	Cerro Tololo, 1m0-05	29.11.2013	<i>i</i>	600 × 2	1.9
ESO 420-G013	Cerro Tololo, 1m0-05	29.11.2013	<i>r</i>	600 × 2	1.8
ESO 423-G024	Siding Spring, 1m0-11	30.11.2013	<i>g</i>	450 × 4	2.6
ESO 423-G024	Siding Spring, 1m0-11	30.11.2013	<i>i</i>	600 × 2	1.7
ESO 423-G024	Siding Spring, 1m0-11	30.11.2013	<i>r</i>	600 × 2	1.8
IC 1608	Cerro Tololo, 1m0-05	29.11.2013	<i>g</i>	450 × 4	1.4
IC 1608	Cerro Tololo, 1m0-05	29.11.2013	<i>r</i>	600 × 2	1.4
IC 1608	Cerro Tololo, 1m0-05	29.11.2013	<i>i</i>	600 × 2	1.5
NGC 216	SAAO, 1m0-12	29.11.2013	<i>g</i>	450 × 4	1.6
NGC 216	SAAO, 1m0-12	29.11.2013	<i>i</i>	600 × 2	2.2
NGC 1210	Cerro Tololo, 1m0-09	29.11.2013	<i>g</i>	450 × 3	1.7
NGC 1210	Cerro Tololo, 1m0-09	29.11.2013	<i>r</i>	600 × 2	1.8
NGC 1210	Cerro Tololo, 1m0-09	29.11.2013	<i>i</i>	600 × 2	2.6
NGC 1930	Cerro Tololo, 1m0-04	30.11.2013	<i>g</i>	450 × 4	2.0
NGC 1930	Cerro Tololo, 1m0-04	30.11.2013	<i>i</i>	600 × 3	2.0
NGC 1930	Cerro Tololo, 1m0-04	30.11.2013	<i>r</i>	600 × 3	1.9
NGC 2267	Cerro Tololo, 1m0-09	30.11.2013	<i>g</i>	450 × 6	1.8
NGC 2267	SAAO, 1m0-12	30.11.2013	<i>g</i>	450 × 4	4.4
NGC 2267	SAAO, 1m0-12	30.11.2013	<i>r</i>	600 × 2	4.5
NGC 2310	Cerro Tololo, 1m0-05	30.11.2013	<i>g</i>	450 × 2	2.1
NGC 2310	Cerro Tololo, 1m0-05	30.11.2013	<i>i</i>	600 × 2	1.9
NGC 2310	Cerro Tololo, 1m0-05	30.11.2013	<i>r</i>	600 × 2	2.1
NGC 6893	Cerro Tololo, 1m0-09	15.11.2013	<i>g</i>	900 × 2	1.4
NGC 6893	Cerro Tololo, 1m0-09	15.11.2013	<i>r</i>	1200 + 600	2.0
NGC 6893	Cerro Tololo, 1m0-09	15.11.2013	<i>i</i>	1200 + 600 + 600	2.0
NGC 7702	Cerro Tololo, 1m0-05	11.11.2013	<i>g</i>	450 × 4	1.5
NGC 7702	Cerro Tololo, 1m0-05	11.11.2013	<i>r</i>	600 × 2	1.5
NGC 7702	Cerro Tololo, 1m0-05	11.11.2013	<i>i</i>	600 × 2	1.7
NGC 7702	Cerro Tololo, 1m0-09	12.11.2013	<i>g</i>	900 × 2	2.0
NGC 7702	Cerro Tololo, 1m0-09	12.11.2013	<i>r</i>	1200	1.4
NGC 7702	Cerro Tololo, 1m0-09	13.11.2013	<i>g</i>	900 × 2	2.5
NGC 7702	Cerro Tololo, 1m0-09	13.11.2013	<i>r</i>	1200	1.4
NGC 7744	Cerro Tololo, 1m0-05	13.11.2013	<i>g</i>	450 × 4	1.7
NGC 7744	Cerro Tololo, 1m0-05	13.11.2013	<i>r</i>	600 × 2	1.7
NGC 7744	Cerro Tololo, 1m0-05	13.11.2013	<i>i</i>	600	1.4

$2 \times 2$  binning, the angular size of each pixel is  $0.47''$ , and each frame covers an area  $15.8' \times 15.8'$  in size. Each SBIG camera can obtain frames in 12 different filters, of which we used the *gri* filters of the Sloan survey [21]. Our observing program was carried out during the commissioning time of the LCOGT, when not all components of the service regime were fully operational. As a result, our data have varying quality, and are not always satisfactory for our task.

Information about the observations that were ultimately used for our analysis is presented in Table 2, which gives the (a) name of the galaxy, (2) the observatories hosting the LCOGT telescopes used to acquire the frames, (3) the date of the observations, (4) the filter, (5) the exposure time and number of images for each observation, and (6) the seeing during the observations.

The primary reduction of the data was carried out automatically for all the LCOGT data obtained, and included:

- 1) masking of bad pixels,
- 2) correction for the zero level (BIAS),
- 3) correction for the dark current (DARK),
- 4) correction for a flat field (FLAT),
- 5) reduction to universal coordinates.

After the primary reduction, the images were analyzed further using mathematical software designed for work with digital images written by Vlasyuk [22]. This software can be used to conduct an isophote analysis, in order to obtain the orientation parameters of the isophotes, construct surface-brightness profiles averaged in azimuth, and analyze the resulting surface-brightness profiles of the disks by obtaining a least-squares fit of their exponents.

### 3. RESULTS OF OUR ANALYSIS OF THE S0 GALAXY STRUCTURES

Figures 1–12 present the results of our analysis of the images of the sample galaxies. The color maps in Fig. 1 are mainly *g–r* maps; only when images of comparable quality were not available in *g* and *r* did we construct maps of *r–i* (NGC 2310) or *g–i* (NGC 216, NGC 6893). The surface-brightness profiles and isophotal parameters in Figs. 2–11 are mainly those for *r*. Since we did not obtain data for photometric standards during the observations, the images were calibrated in the SDSS magnitude system using aperture electrophotometric data; the HYPERLEDA database contains aperture electrophotometry data primarily in the Johnson–Cousins system. Most of the photoelectric data were obtained in [23, 24]. We translated these *BVRI* magnitudes into the SDSS system using the corresponding equations from [25]. The HYPERLEDA database did

not contain aperture photometry data for the three galaxies ESO 420-G013, IC 1608, and NGC 1210, and the zero points for both the color maps and the brightness profiles were chosen arbitrarily.

We chose the range of radii where the exponential part of the radial surface-brightness distribution dominates. If a flat maximum with a constant position angle in the ellipticity isophotes was observed in this same range of radii, we conclude that this region is dominated by an inner circular, relatively thin stellar disk. Note that we can estimate the thickness of the disk separately using our new method [12], which is applicable precisely for circular, exponential disks viewed far from edge-on.

Further, we describe the individual properties of each galaxy.

**ESO 058-G019.** This moderate-luminosity galaxy has no visible bar. It is a member of a small, diffuse group, but the only nearby companion is a factor of ten weaker. The body of the galaxy displays a uniform red color, but the nucleus is relatively blue (Fig. 1). The exponential disk begins to dominate from  $R = 14''$  (3.8 kpc). We observe a break in the profile at  $R \approx 30''$  (8 kpc), beyond which an outer exponential disk with a longer scale is visible. According to the classification of [4], this is a Type III (anti-truncated) profile.

**ESO 420-G013.** This is a very compact galaxy viewed nearly face-on (the optical radius is roughly half the radii of the other galaxies in our sample with similar luminosities). There are no nearby companions down to luminosities of 1% of the galaxy, and it has been classified as a very isolated galaxy [26]. It is noted in the IRAS survey as having appreciable flux at  $12 \mu\text{m}$  [27], and a compact radio source that is unresolved on scales of  $5''$  is present in the nucleus [28]. However, it is not possible to firmly classify this as an active nucleus: according to its optical spectrum, these features are most likely associated with a nuclear starburst [29]. Indeed, a blue nucleus and open dust ring with a radius of less than  $5''$  are visible in our color map. Since the galaxy is viewed face-on, it is not possible to identify the boundary between the bulge and disk based on the isophote-ellipticity profile. Two quasi-exponential sections beyond the dust ring ( $R > 5''$ ) are visible in the surface-brightness profile; we took the outer of these ( $R > 10''$ ) to represent the disk, and have analyzed this region.

**ESO 423-G024.** This is a classical giant lenticular galaxy with a prominent red nucleus. Although various catalogs classify it as a lenticular galaxy, and our surface photometry reliably extends to the optical boundary of the galaxy, no exponential disk is visible in the surface-brightness profile. The ellipticity profile

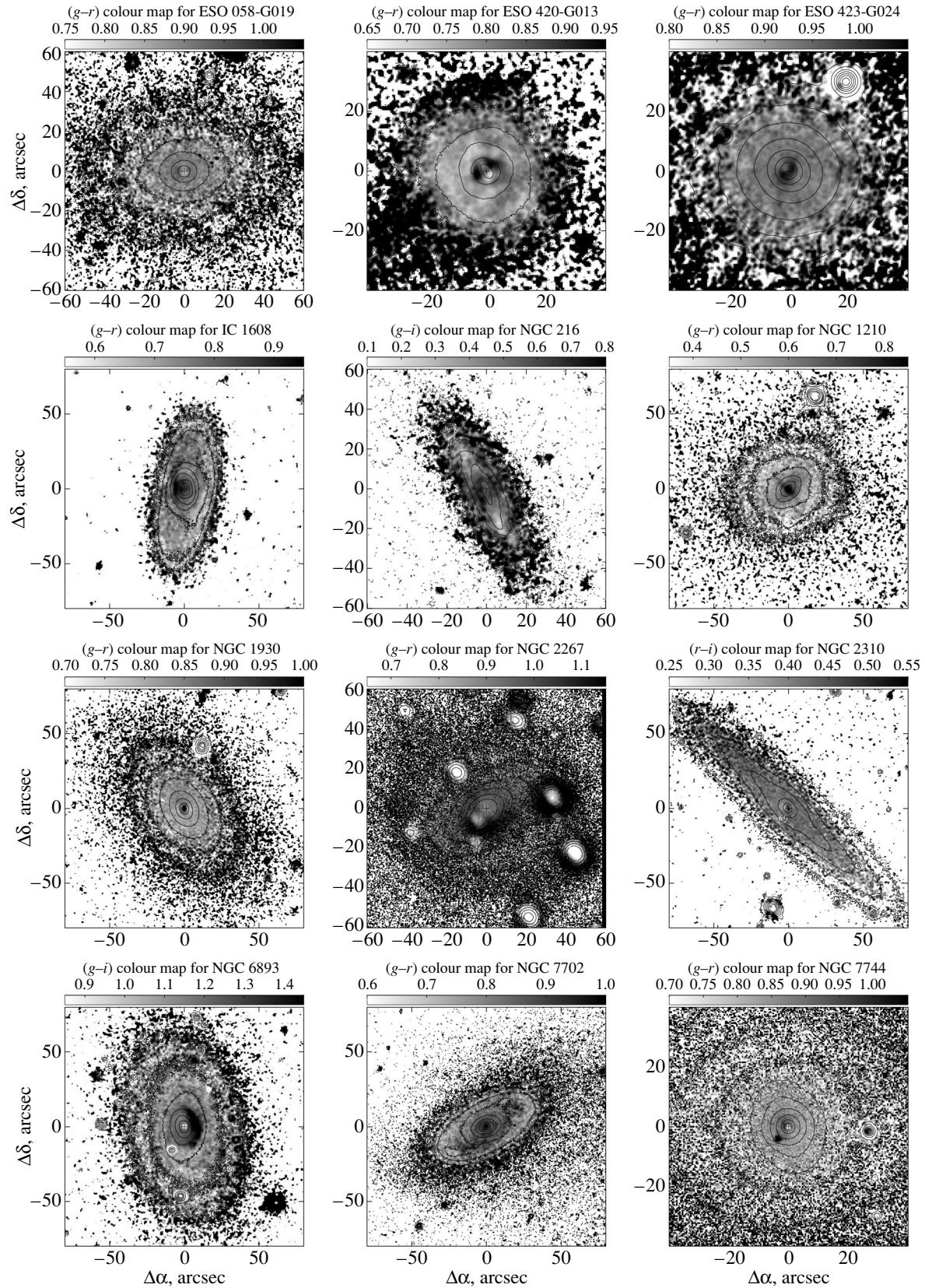


**Fig. 1.** Color maps constructed for the studied galaxies. The color maps for ESO 420-G013, NGC 1210, and IC 1608 have an arbitrary zero point due to the absence of calibration information. The spatial resolution was artificially degraded to the worse of the two filters. The orientation of the images is such that North is upward and East is to the left; the coordinate origin coincides with the nucleus of each galaxy. Contours for the redder of the two filters are superposed onto each color map (gray scale).

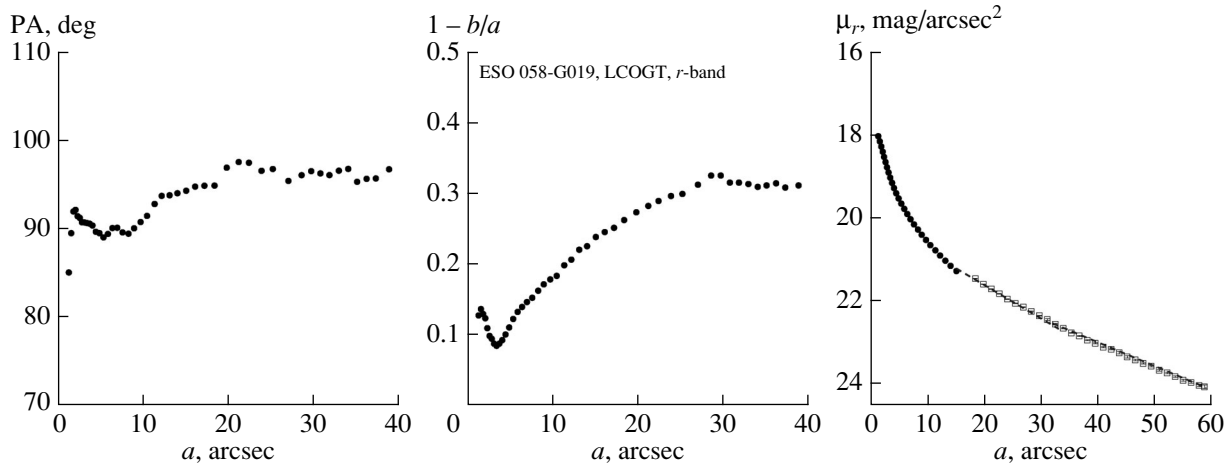


**Fig. 2.** ESO 058-G019: radial distributions of the position angle of the isophote major axis (left), the isophote ellipticity (center), and the surface brightness in the  $r$  band (right). The dark circles in the right panel depict the profile calculated from an isophote analysis, and the squares the profile calculated from azimuthal averaging of the surface brightness inside ellipses whose orientation and axial ratio was fixed in accordance with the outermost parameters derived from an isophote analysis. The dashed line shows a model exponential disk profile fitted to individual sections of the observed brightness profile.

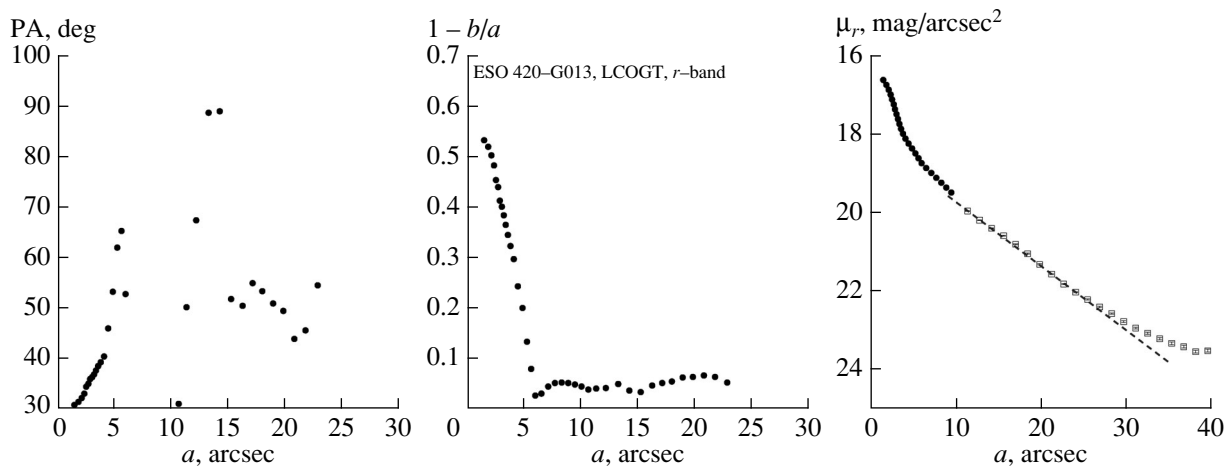


**Fig. 3.** ESO 420-G013: radial distributions of the position angle of the isophote major axis (left), isophote ellipticity (center), and surface brightness in the  $r$  band (right). The zero point of the surface-brightness profile is arbitrary. The filled circles in the right-hand panel depict the profile calculated using an isophote analysis, and the squares the profile calculated through azimuthal averaging of the surface brightness inside ellipses with their orientation and axial ratio fixed in accordance with the outermost parameters derived through the isophote analysis. The dashed line shows the model exponential profile of the disk fitted in individual sections of the observed brightness profile.

does not grow beginning from  $R \approx 15''$ , but this is not very indicative, since the orientation of the galaxy is such that it is viewed nearly face-on. We analyzed two short, formally exponential radial segments as a possible disk, whose extent does not exceed 1.5 exponential scales:  $R = 15'' - 30''$  and  $R = 35'' - 66''$ .

**IC 1608.** This galaxy has a rich morphology: catalogs note the presence of an inner and outer ring, while a bar is absent. In our color map, the inner ring is distinguished by a concentration of dust—red colors on one side of the nucleus. The brightness profile is completely flat at  $R = 20'' - 40''$ , forming a

so-called lens or broad ring. Both the ellipticity and the position angle of the isophote major axis change inside this radius interval, presumably due to a disruption of axial symmetry (typical for a lens) or the presence of faint spirals, which can be noted from their blue color in our map in Fig. 1. As the inner and outer exponential disks, we analyzed a small interval of radii inside and outside the lens.

**NGC 216.** This is a dwarf S0 galaxy viewed edge-on. According to the NED database, Haro [30] noted that the galaxy is very blue, and that its spectrum contains strong emission lines. Bottinelli et

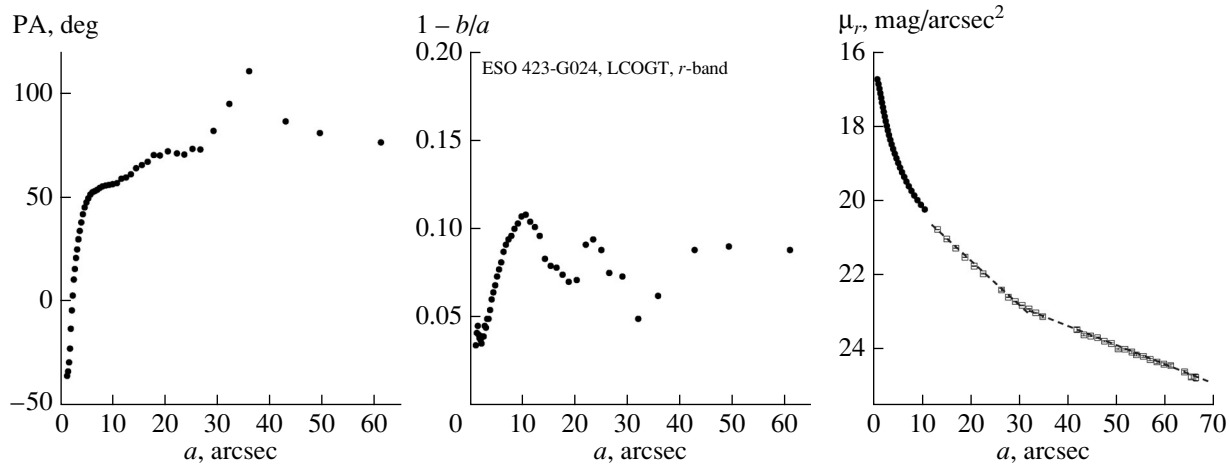


**Fig. 4.** ESO 423-G024: radial distributions of the position angle of the isophote major axis (left), isophote ellipticity (center), and surface brightness in the  $r$  band (right). The filled circles in the right-hand panel depict the profile calculated using an isophote analysis, and the squares the profile calculated through azimuthal averaging of the surface brightness inside ellipses with their orientation and axial ratio fixed in accordance with the outermost parameters derived through the isophote analysis. The dashed line shows the model exponential profile of the disk fitted in individual sections of the observed brightness profile.

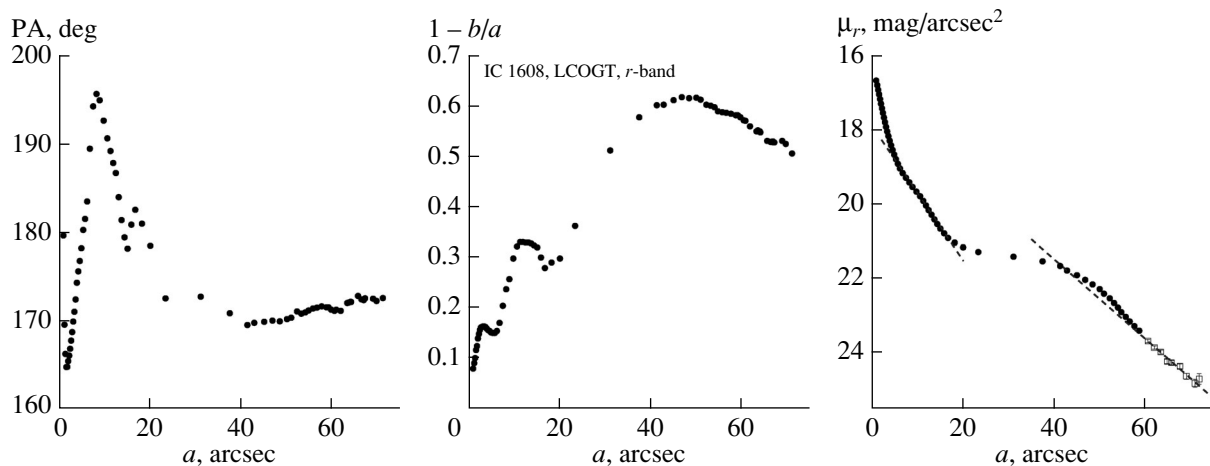


**Fig. 5.** IC 1608: radial distributions of the position angle of the isophote major axis (left), isophote ellipticity (center), and surface brightness in the  $r$  band (right). The zero point of the surface-brightness profile is arbitrary. The filled circles in the right-hand panel depict the profile calculated using an isophote analysis, and the squares the profile calculated through azimuthal averaging of the surface brightness inside ellipses with their orientation and axial ratio fixed in accordance with the outermost parameters derived through the isophote analysis. The dashed line shows the model exponential profile of the disk fitted in individual sections of the observed brightness profile.

al. [31] deduced the presence of a huge amount of gas in the galaxy:  $2 \times 10^9 M_{\odot}$  of neutral hydrogen, with a surface density far exceeding the threshold of Kennicutt [32]. Naturally, vigorous star formation is occurring in the galaxy—judging from the color map of Fig. 1, in both the nucleus and in the extended thin disk. Since the galaxy is viewed edge-on, we did not carry out an isophote analysis, and the brightness profile was constructed within a one-dimensional cut along the equator (Fig. 12). Judging from this profile, the bulge is completely absent, and a north–south asymmetry in the brightness distribution of the stellar

disk is visible at radii  $R = 5'' - 40''$ . In an edge-on galaxy, this could represent either spiral arms or a thin bar; both formations will tend to collect dust in shocks at the edge.

**NGC 1210.** The galaxy has a feature generally acknowledged to be a bar, as well as a pair of less confidently classified rings. A curious feature is visible in the color map in Fig. 1: a narrow, red (dust) band along the minor axis of the bar in the center of the galaxy, which can be traced in our color map to radii  $12'' - 15''$  from the nucleus. It appears that the gas in the very center of the galaxy is distributed in and

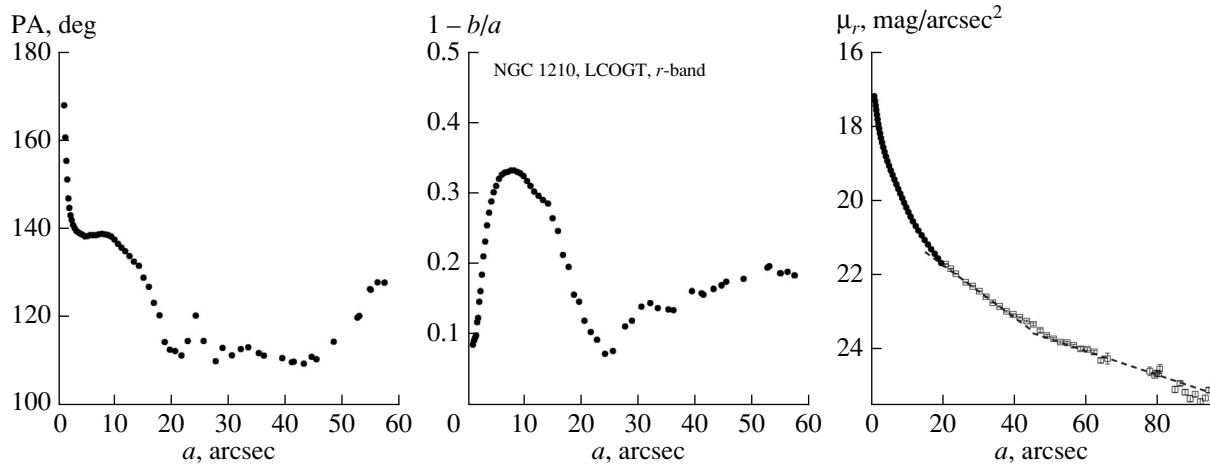


**Fig. 6.** NGC 1210: radial distributions of the position angle of the isophote major axis (left), isophote ellipticity (center), and surface brightness in the  $r$  band (right). The zero point of the surface-brightness profile is arbitrary. The filled circles in the right-hand panel depict the profile calculated using an isophote analysis, and the squares the profile calculated through azimuthal averaging of the surface brightness inside ellipses with their orientation and axial ratio fixed in accordance with the outermost parameters derived through the isophote analysis. The dashed line shows the model exponential profile of the disk fitted in individual sections of the observed brightness profile.

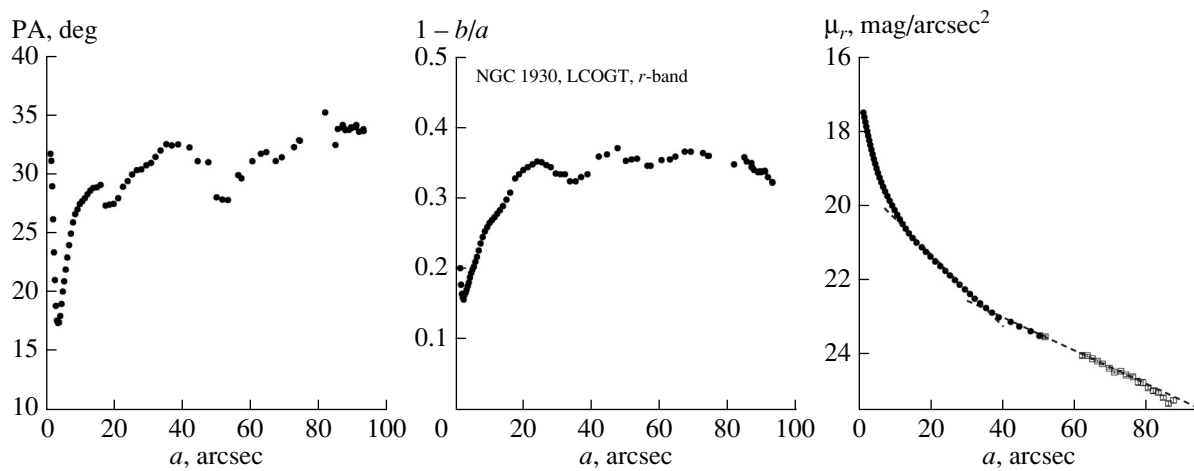


**Fig. 7.** NGC 1930: radial distributions of the position angle of the isophote major axis (left), isophote ellipticity (center), and surface brightness in the  $r$  band (right). The filled circles in the right-hand panel depict the profile calculated using an isophote analysis, and the squares the profile calculated through azimuthal averaging of the surface brightness inside ellipses with their orientation and axial ratio fixed in accordance with the outermost parameters derived through the isophote analysis. The dashed line shows the model exponential profile of the disk fitted in individual sections of the observed brightness profile.

rotates in a plane that is polar relative to the plane of the stellar disk and bar. The large amount of gas contained by the galaxy was noted earlier: Shiminovich et al. [33] mapped a peculiar ring of neutral hydrogen passing through the galactic nucleus, and Marino et al. [34] detected an ultraviolet signal and a star-forming region in partial arcs of this ring. Our surface-brightness profile shows an excess at distances from the center exceeding  $40''$ ; reversal of the position angle of the isophote major axis is also visible there (Fig. 6). The outer ring may have a non-circular shape, or it may have formed outside the main plane of

the galactic disk as a result of the accretion of external gas and subsequent star formation. We analyzed the exponential stellar disk at radii  $R = 25'' - 40''$ , and also an exponential section of the profile with very low surface brightness beyond the outer ring ( $R = 50'' - 80''$ ), for which we were not able to measure the thickness.

**NGC 1930.** This giant lenticular galaxy is the least isolated in our sample, and is a member of a wide triplet. The galaxy is somewhat red throughout, and the nucleus is very red. The isophotes do not show any distortion due to the influence of tidal interactions

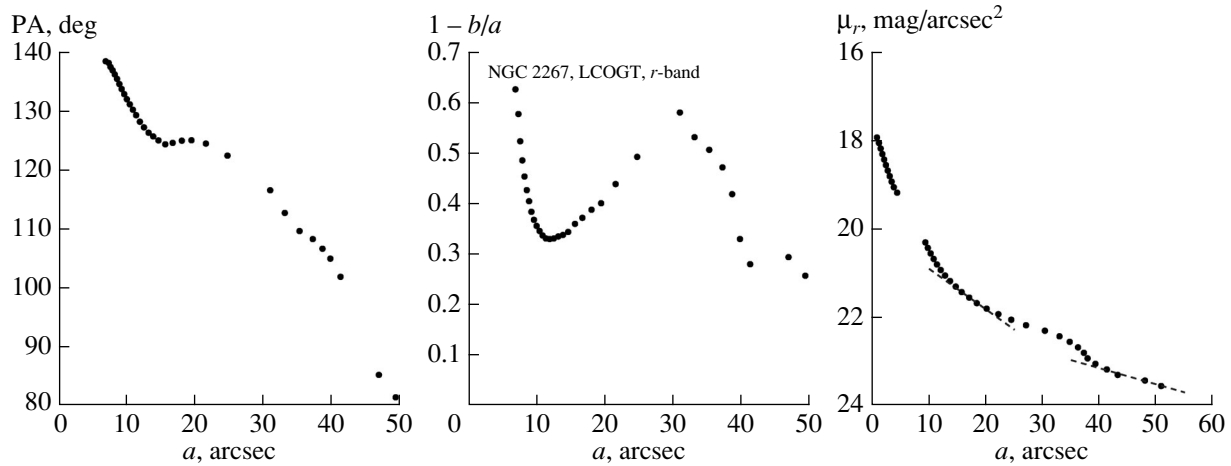


**Fig. 8.** NGC 2267: radial distributions of the position angle of the isophote major axis (left), isophote ellipticity (center), and surface brightness in the  $g$  band (right). The filled circles in the right-hand panel depict the profile calculated using an isophote analysis. The dashed line shows the model exponential profile of the disk fitted in individual sections of the observed brightness profile.

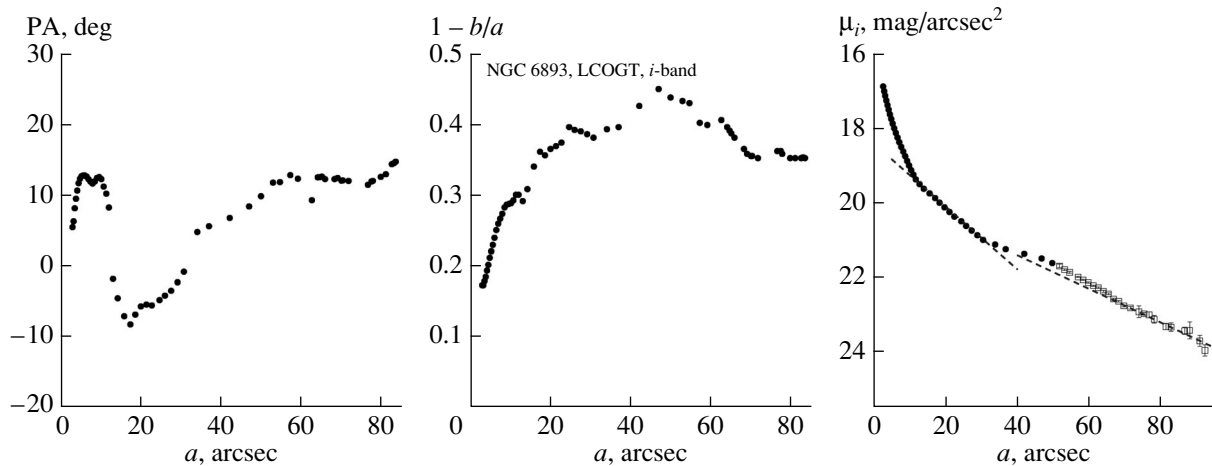


**Fig. 9.** NGC 6893: radial distributions of the position angle of the isophote major axis (left), isophote ellipticity (center), and surface brightness in the  $i$  band (right). The filled circles in the right-hand panel depict the profile calculated using an isophote analysis, and the squares the profile calculated through azimuthal averaging of the surface brightness inside ellipses with their orientation and axial ratio fixed in accordance with the outermost parameters derived through the isophote analysis. The dashed line shows the model exponential profile of the disk fitted in individual sections of the observed brightness profile.

or dust. Beginning from a radius of roughly  $15''$ , the profile of the isophote parameters (Fig. 7) displays flat dependences for the ellipticity and the position angle of the major axis, suggesting dominance of a disk. The profile of the disk surface brightness is regular and two-tiered (anti-truncated); we determined the structural parameters for both tiers. A drop in the brightness profile can be seen at  $R \approx 85''$  (23.5 kpc).

**NGC 2267.** This galaxy has a large-scale bar and an inner red ring. A bright blue star is located  $7''$  from the center, which distorts the surface-brightness profiles and isophote parameters out to distances of  $10''$  from the center. The region of dominance of the

exponential disk may be manifest only at  $R > 40''$ : only here does the isophote-ellipticity profile emerge onto a plateau. This is the region we analyzed as the disk, but it was not possible to measure the disk thickness here due to the low surface brightness. It is possible that the inclination and thickness measured formally for an inner exponential section of the profile at radii  $R = 14'' - 21''$  bears no relationship to the real orientation of the disk in space, since the axial symmetry of the surface-brightness distribution could be disrupted due to the bar; our method for measuring the inclination and thickness is not suitable for such disks.

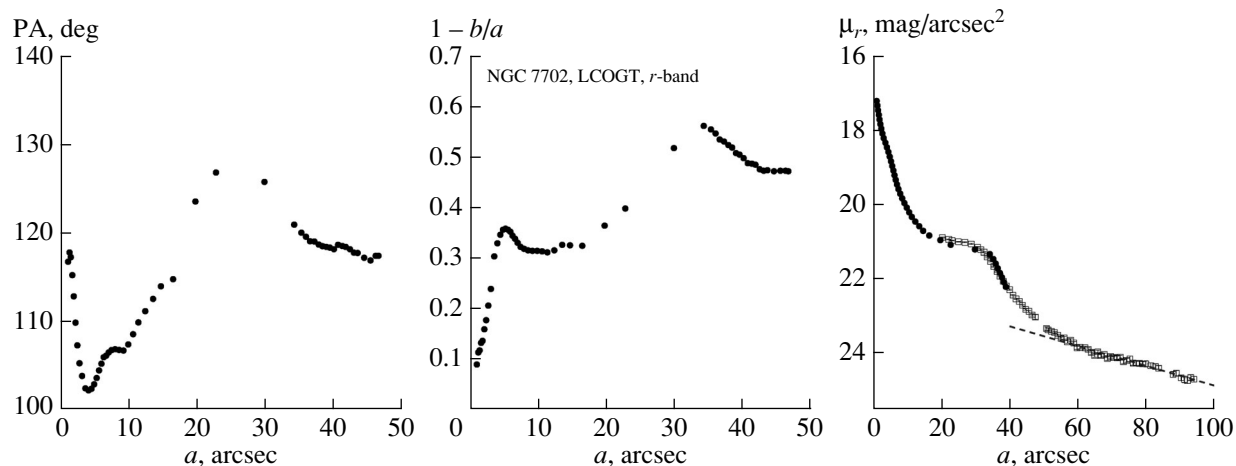


**Fig. 10.** NGC 7702: radial distributions of the position angle of the isophote major axis (left), isophote ellipticity (center), and surface brightness in the  $r$  band (right). The filled circles in the right-hand panel depict the profile calculated using an isophote analysis, and the squares the profile calculated through azimuthal averaging of the surface brightness inside ellipses with their orientation and axial ratio fixed in accordance with the outermost parameters derived through the isophote analysis. The dashed line shows the model exponential profile of the disk fitted in individual sections of the observed brightness profile.

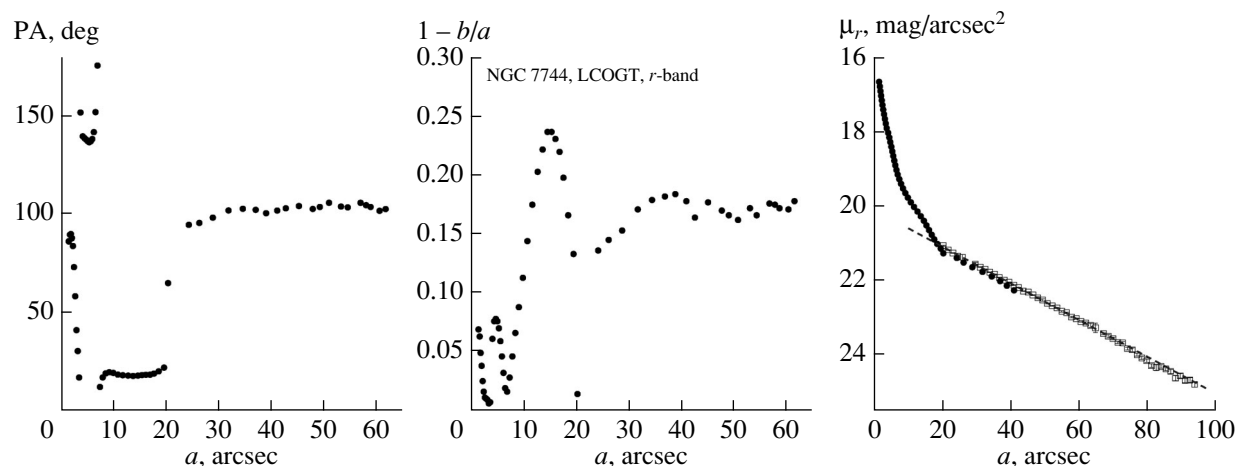


**Fig. 11.** NGC 7744: radial distributions of the position angle of the isophote major axis (left), isophote ellipticity (center), and surface brightness in the  $r$  band (right). The filled circles in the right-hand panel depict the profile calculated using an isophote analysis, and the squares the profile calculated through azimuthal averaging of the surface brightness inside ellipses with their orientation and axial ratio fixed in accordance with the outermost parameters derived through the isophote analysis. The dashed line shows the model exponential profile of the disk.

**NGC 2310.** This nearby lenticular galaxy is viewed strictly edge-on. It is included in the 2MIG catalog of isolated galaxies [35]. Two blue spots located symmetrically about the center at distances of two to three arcseconds in a direction inclined to the major axis are visible in our color map. The color and surface-brightness profiles along the major axis (Fig. 12) are very asymmetric. A lens, or more likely large-scale bar, is clearly visible in the surface-brightness profile: in the latter case, the asymmetry of the surface-brightness profile could be due to a concentration of dust at the inner edge of the bar.

**NGC 6893.** This galaxy has no bar, but does

have a set of rings. The inner ring, with a radius of about  $13''$ , is inclined to the plane of the galaxy, as is indicated by the reversal of the isophote major axis at this radius and the open red (dust) arc. Further, an inner exponential disk is visible, and another very broad ring of enhanced brightness lying in the plane of the disk begins at a distance  $R > 35''$  from the center. An outer exponential disk with a sharp cutoff can be seen at  $R > 70''$ .

**NGC 7702.** This is another galaxy with no bar, but having a set of rings. It is very isolated—there are no any dwarf galaxies with luminosities brighter than

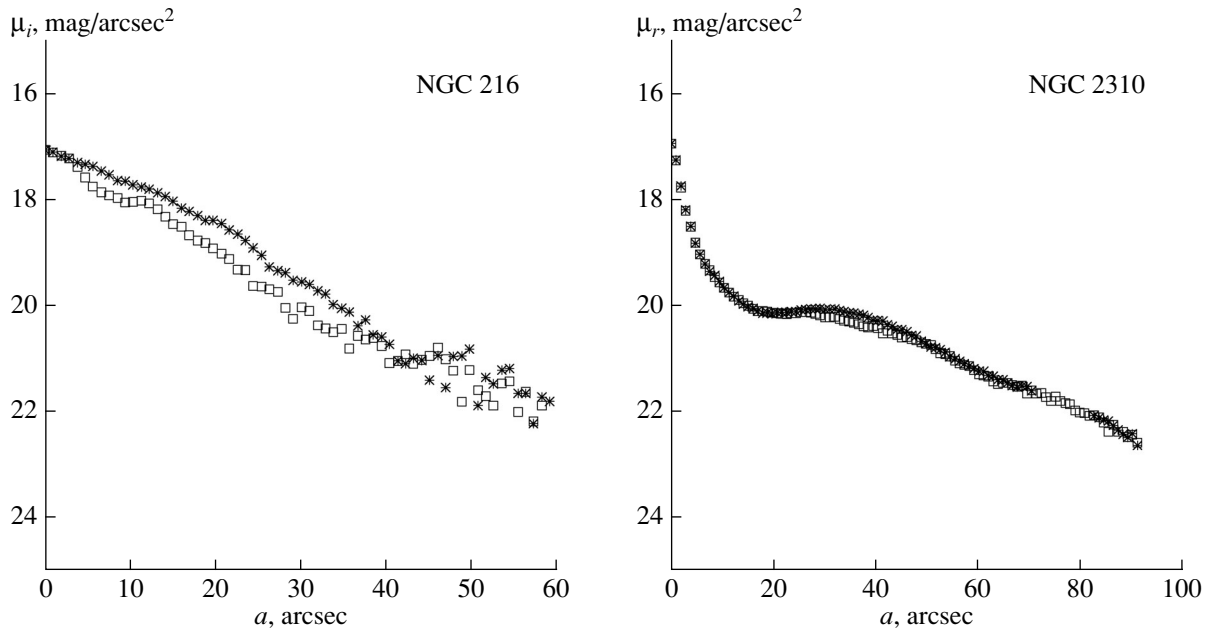


**Fig. 12.** Radial distributions of the surface brightness for the two edge-on galaxies NGC 216 (left) and NGC 2310 (right). One-dimensional cuts through the images were obtained along the disk equators. Different symbols are used to trace the two halves of the galaxy on either side of the nucleus.

half a percent the luminosity of NGC 7702 within 750 kpc of the galaxy. A plateau is observed in the brightness profile beyond the central region, at  $R > 10''$ , which is usually associated with the presence of a so-called lens. However, if we consider the color map, it becomes clear that the outer part of the lens (near  $R = 30'' - 35''$ ) is a broad, blue ring, inside of which we observe a complex structure resembling short, thick, red (dust?) spirals. The flat shape of the surface-brightness profile inside the outer ring cannot be explained by absorption by dust: a sharp cut-off in the profile with an exponential scale of only 1 kpc is observed outside the ring. In his detailed photometric study of NGC 7702, Buta [36] traced the surface-brightness profile deeper than we have, approximately to  $28''$  in the  $B$  filter; his profile emerges onto a quite normal exponential disk at radii  $R > 70''$ . The shape of the profile inside this radius forms a series of dips and rises relative to the inward interpolation of the exponential law, suggesting a radial redistribution of matter and a concentration of star formation in a series of annular zones. Given that the galaxy has no bar and is completely isolated, the mechanism giving rise to this strong redistribution of matter is currently a mystery.

**NGC 7744.** This isolated galaxy probably has a bar: the isophotes at  $R = 8'' - 20''$  are turned  $90^\circ$  to the isophotes of the outer disk. The surface-brightness profile in this range of radii is however steep and exponential, in contrast to the typical flat

brightness profiles of bars in early-type galaxies, suggesting the presence of an inclined disk, given the clear asymmetry in the color distribution at the center of the galaxy. At radii greater than  $R > 20''$  and out to the optical edge of the galaxy, we observe a quite regular disk, with constant ellipticity and major-axis position angle of the isophotes.

Table 3 presents quantitative results of our analysis of the disk structures of the galaxies viewed at angles less than or equal to  $70^\circ$ . We developed an algorithm suitable for such disk orientations that enables determination of both the exponential scale of the radial surface-brightness distribution, and the relative thickness of the disk  $q$  as defined by Hubble [37]. The essence of this method [12] is that we determine the intrinsic inclination of the galactic disk to the line of sight  $i$ , assuming it is axially symmetric, from the azimuthal run of the radial exponential scale, then compare  $1 - \cos i$  with the isophote ellipticity, which is always less than  $1 - \cos i$  due to the finite thickness of the disk. In addition to the parameters of the exponential disks—the central surface brightness and radial scale—Table 3 also presents the intrinsic inclination of each disk to the line of sight and the relative thickness of the disk. We were not able to determine the disk thickness for five outer disks, due to insufficient signal (NGC 2267, ESO 058-G019) or low surface brightness (NGC 6893, NGC 1210, NGC 7702).

**Table 3.** Disk parameters calculated for the galaxies studied.

Galaxies	$\Delta R$	$\Delta R$ , kpc	$h$	$h$ , kpc	$\mu_{0,r}$ , mag/arcsec	$i$	$q$	Structures	Location of structures $R_{r,l,bar,br}$
ESO 058-G019	18''–28''	4.8–7.5	$13.5'' \pm 0.1''$	3.6	20.0	$53.7^\circ \pm 0.4^\circ$	$0.43 \pm 0.02$	upward break	30''
	35–55	9.4–14.7	$19.0 \pm 0.0$	5.1	20.7	–	–		
ESO 420-G013	10–25	2.3–5.8	$6.62 \pm 0.05$	1.5	18.1::	$40 \pm 3$	$0.64 \pm 0.18$	ring	5
ESO 423-G024	15–30	3.75–7.5	$9.0 \pm 0.0$	2.3	19.2	$26.2 \pm 0.7$	$0.67 \pm 0.04$		
	35–66	8.8–16.5	$21.0 \pm 0.5$	5.2	21.3	$50 \pm 4$	$0.40 \pm 0.01$		
IC 1608	7–17	1.6–3.9	$6.0 \pm 0.1$	1.4	17.9::	$64.5 \pm 1.0$	$0.49 \pm 0.02$	ring	7
	47–67	10.7–15.3	$10.15 \pm 0.13$	2.3	17.2::	$71.5 \pm 1.5$	$0.28 \pm 0.02$	lens	20–40
NGC 1210	25–40	6.3–10.1	$15.3 \pm 0.3$	3.9	20.3	$43 \pm 0.5$	$0.52 \pm 0.04$	bar	8
	50–80	12.6–20.2	$33.6 \pm 2.0$	8.5	22.1	–	–	ring	52
NGC 1930	12–32	3.3–8.8	$11.3 \pm 0.1$	3.1	19.4	$56.0 \pm 0.6$	$0.40 \pm 0.01$		
	40–77	11–21	$24.2 \pm 0.0$	6.7	21.2	$57.4 \pm 1.0$	$0.37 \pm 0.01$	break	85
NGC 2267	14–21	1.2–1.8	$11.9 \pm 0.6$	1.0	18.8	$68 \pm 4$	$0.41 \pm 0.01$	ring	12
	40–52	3.5–4.5	$30.1 \pm 3.2$	2.6	21.7	–	–	ring	31
NGC 2310*	0–91.5	0–5.7	32.0	2.0	17.04(H)	90	0.22	ring	33
NGC 6893	12–32	2.4–6.4	$12.9 \pm 1.3$	2.6	18.4(i)	$65 \pm 5$	$0.38 \pm 0.07$	ring	13
	67–90	13.4–18.0	$24.0 \pm 1.2$	4.8	19.6(i)	–	–	ring	35–70
NGC 7702	70–95	14.6–19.8	$41.2 \pm 4.0$	8.6	22.2	–	–	ring	30–35
NGC 7744	25–75	5.1–15.3	$22.0 \pm 0.0$	4.5	20.1	$56.3 \pm 0.4$	$0.64 \pm 0.02$	lens	10–20

\* Result of the decomposition of Mosenkov et al. [38] based on the 2MASS data in the  $H$  band.

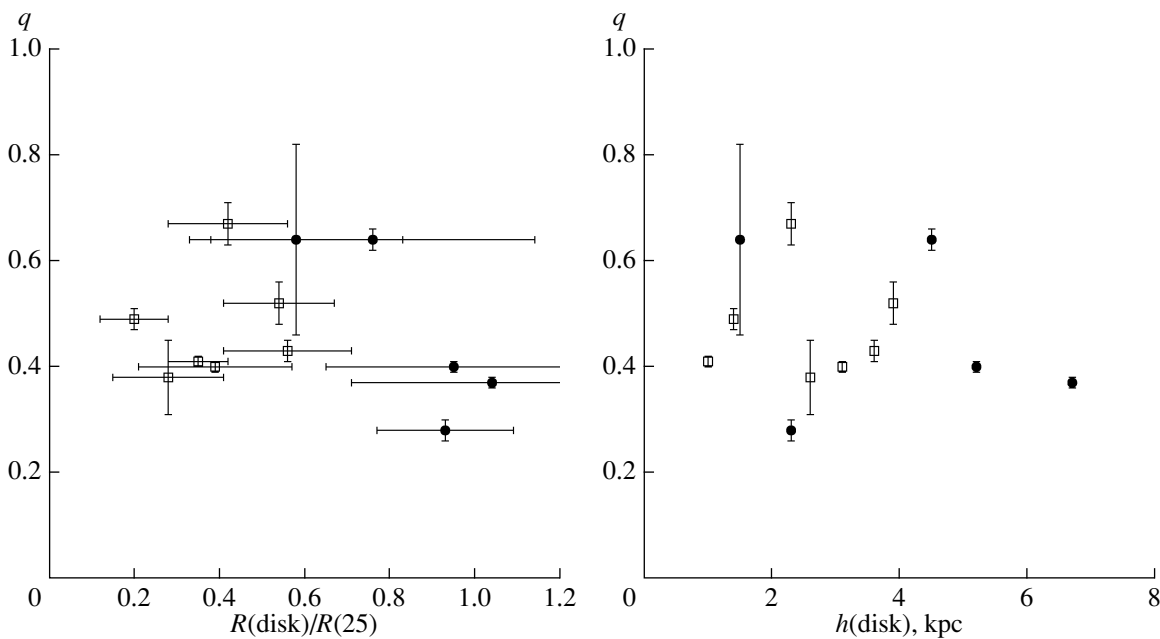
#### 4. DISCUSSION

Table 3 and Fig. 13 present the relative disk thicknesses for the studied galaxies. We can see that there are nearly no thin disks: the objects are concentrated around  $q = 0.4$ . This is not surprising: the mean relative disk thickness for S0 galaxies for the complete sample of Mosenkov et al. [38] was 0.34, albeit with an appreciably greater scatter. However, the group of three disks concentrated near  $q = 0.65$  is of interest. Do these extremely thick disks differ in some other properties? Although the inner disk in ESO 423-G024 could be reclassified as a fat pseudobulge, the thick disks in ESO 420-G013 and NGC 7744 correspond to the only exponential segments, and reach the optical edges of the galaxies, extending over more than two exponential scales.

We tried to test for a possible relationship between the relative thickness of the disk and the distance from the center of the galaxy at which the thickness was measured; i.e., to search for so-called “flaring” of the disk toward its edge. We also compared the relative disk thickness with the characteristic radial

exponential scale characterizing the size of the disk as a whole. The dependences in Fig. 13 are complex, but self-consistent: the maximum thicknesses occur in medium-sized disks and are measured either at distances of about 4–8 kpc from the center or half way to the edge of the galaxy, at 40–70% of the optical size of the galaxy  $R_{25}$ . Both close to the center and at large radii, exceeding 10 kpc or close to  $R_{25}$ , the disks appear, on average, thinner. One somewhat speculative explanation for this dependence could be that we observe flaring of the disks at radii of 2–8 kpc, associated with a radial decrease of the stabilizing effect of the spheroidal subsystem (bulge) on the disk, while the outermost parts of the disks probably formed relatively recently from cool gas (in an “inside–out” scenario for the formation of galactic disks), so that their stellar component, which inherited the velocity dispersion of the parent gas clouds, had no time to become dynamically heated.

The next-to-last column in Table 3 gives some impression of the frequency of encountering various disk substructures in the studied S0 galaxies



**Fig. 13.** Correlation of the relative disk thickness with other parameters of the disk—the radius at which the thickness is measured in units of the total optical radius of the galaxy and the characteristic exponential scale  $h$ . The filled circles depict the outer (or only) disk and the squares the inner disk.

in sparse environments. We noted inner or outer rings in 7 of the 12 studied galaxies. This frequency (58%) is consistent with the statistics of the AR-RAKIS catalog of ring structures, where the presence of stellar rings was noted in 60% of the disks of S0 galaxies in all types of environments, based on the results of the S4G infrared survey [39]. In two of our galaxies, we see a pronounced drop in the radial surface-brightness profile; again, this is expected, since we are considering here isolated S0 galaxies, and not S0 galaxies in clusters, where disks with cut-off are not encountered [13, 14]. In contrast, the fact that we find only two lenses in our sample is somewhat unexpected: it is generally believed that lenses are encountered frequently in S0 galaxies [40], and that they are a typical S0 morphological feature. S0 galaxies with lenses are clearly a minority in our sample. We could try to explain this as an effect of our deeper than average surface photometry: inspection of the incomplete brightness profiles of NGC 2267 or NGC 6893, one could suppose the presence of lenses in these galaxies. However, when we extend the surface-brightness profile somewhat further from the center, it becomes clear that we are dealing with very broad rings, rather than lenses. This uncertainty in the classification of substructures in relatively shallow data can create a situation where rings are mistaken for lenses.

#### ACKNOWLEDGMENTS

This work has made use of the LCOGT telescope network. We thank A. Tekola for help in organizing the observations on telescopes of this network during their commissioning period. We also thank the anonymous referee, whose attentive reading of the paper and valuable comments have helped appreciably improve our presentation of these results. We acknowledge the usage of the HyperLeda database (<http://leda.univ-lyon1.fr>). This research has made use of the NASA/IPAC Extragalactic Database (NED) which is operated by the Jet Propulsion Laboratory, California Institute of Technology, under contract with the National Aeronautics and Space Administration. This work was supported by the Russian Science Foundation (project 14-22-00041).

#### REFERENCES

1. K. C. Freeman, *Astrophys. J.* **160**, 767 (1970).
2. Y. C. Andredakis and R. H. Sanders, *Mon. Not. R. Astron. Soc.* **267**, 283 (1994).
3. Y. C. Andredakis, R. F. Peletier, and M. Balcells, *Mon. Not. R. Astron. Soc.* **275**, 874 (1995).
4. P. Erwin, J. E. Beckman, and M. Pohlen, *Astrophys. J.* **626**, L81 (2005).
5. P. Erwin, M. Pohlen, and J. E. Beckman, *Astron. J.* **135**, 20 (2008).
6. M. Pohlen and I. Trujillo, *Astron. Astrophys.* **454**, 759 (2006).

7. J. D. Younger, T. J. Cox, A. C. Seth, and L. Hernquist, *Astrophys. J.* **670**, 269 (2007).
8. A. Borlaff, M. C. Eliche-Moral, C. Rodríguez-Pérez, M. Querejeta, T. Tapia, A. Borlaff, M. C. Eliche-Moral, C. Rodríguez-Pérez, M. Querejeta, T. Tapia, P. G. Pérez-González, J. Zamorano, J. Gallego, and J. Beckman, *Astron. Astrophys.* **570**, A103 (2014).
9. C. Firmani and V. Avila-Reese, *Mon. Not. R. Astron. Soc.* **315**, 457 (2000).
10. D. N. C. Lin and J. E. Pringle, *Astrophys. J. Lett.* **320**, L87 (1987).
11. A. D. Slyz, J. E. Devriendt, J. Silk, and A. Burkert, *Mon. Not. R. Astron. Soc.* **333**, 894 (2002).
12. E. M. Chudakova and O. K. Sil'chenko, *Astron. Rep.* **58**, 281 (2014).
13. P. Erwin, L. Gutiérrez, and J. E. Beckman, *Astrophys. J.* **744**, L11 (2012).
14. D. T. Maltby, A. Aragón-Salamanca, M. E. Gray, C. Hoyos, Ch. Wolf, S. Jogee, and A. Böhm, *Mon. Not. R. Astron. Soc.* **447**, 1506 (2015).
15. L. Gutiérrez, P. Erwin, R. Aladro, and J. E. Beckman, *Astron. J.* **142**, A145 (2011).
16. E. Laurikainen, H. Salo, R. Buta, J. H. Knapen, and S. Comerón, *Mon. Not. R. Astron. Soc.* **405**, 1089 (2010).
17. O. K. Sil'chenko, I. S. Proshina, A. P. Shulga, and S. E. Koposov, *Mon. Not. R. Astron. Soc.* **427**, 790 (2012).
18. E. J. Johnston, A. Aragón-Salamanca, and M. R. Merrifield, *Mon. Not. R. Astron. Soc.* **441**, 333 (2014).
19. G. de Vaucouleurs, A. de Vaucouleurs, H. G. Corwin, Jr., G. de Vaucouleurs, A. de Vaucouleurs, H. G. Corwin, Jr., R. J. Buta, G. Paturel, and P. Fouqué, *Third Reference Catalog of Bright Galaxies*, Vol. 1: *Explanations and References* (Springer, New York, 1991).
20. T. M. Brown, N. Baliber, F. B. Bianco, M. Bowman, B. Burleson, P. Conway, M. Crellin, É. Depagne, J. De Vera, B. Dilday, D. Dragomir, M. Dubberley, J. D. Eastman, M. Elphick, M. Falarski, et al., *Publ. Astron. Soc. Pacif.* **125**, 1031 (2013).
21. M. Fukugita, T. Ichikawa, J. E. Gunn, M. Doi, K. Shimasaku, and D. P. Schneider, *Astron. J.* **111**, 1748 (1996).
22. V. V. Vlasyuk, *Astrofiz. Issled. (Izv. SAO RAN)* **36**, 107 (1993).
23. A. Lauberts, *Astron. Astrophys. Suppl. Ser.* **58**, 249 (1984).
24. P. Poulain, *Astron. Astrophys. Suppl. Ser.* **72**, 215 (1988).
25. K. Jordi, E. K. Grebel, and K. Ammon, *Astron. Astrophys.* **460**, 339 (2006).
26. I. D. Karachentsev, D. I. Makarov, V. E. Karachentseva, and O. V. Melnyk, *Astrophys. Bull.* **66**, 1 (2011).
27. B. Rush, M. A. Malkan, and L. Spinoglio, *Astrophys. J. Suppl. Ser.* **89**, 1 (1993).
28. J. J. Condon, G. Helou, D. B. Sanders, and B. T. Soifer, *Astrophys. J. Suppl. Ser.* **103**, 81 (1996).
29. L. J. Kewley, C. A. Heisler, M. A. Dopita, and S. Lumsden, *Astrophys. J. Suppl. Ser.* **132**, 37 (2001).
30. G. Haro, *Bol. Observ. Tonantzintla Tacubaya* **2** (14), 8 (1956).
31. L. Bottinelli, P. Chamaraux, L. Gouguenheim, and J. Heidmann, *Astron. Astrophys.* **29**, 217 (1973).
32. R. C. Kennicutt, Jr., *Astrophys. J.* **344**, 685 (1989).
33. D. Schiminovich, J. H. van Gorkom, M. Dijkstra, Y. Li, A. Petric, and J. M. van der Hulst, in *Gas and Galaxy Evolution*, Ed. by J. E. Hibbard, M. Rupen, and J. H. van Gorkom, *ASP Conf. Ser.* **240**, 864 (2001).
34. A. Marino, E. Iodice, R. Tantalò, L. Piovan, D. Bettoni, L. M. Buson, C. Chiosi, G. Galletta, R. Rampazzo, and R. M. Rich, *Astron. Astrophys.* **508**, 1235 (2009).
35. V. E. Karachentseva, S. N. Mitronova, O. V. Melnyk, and I. D. Karachentsev, *Astrophys. Bull.* **65**, 1 (2010).
36. R. Buta, *Astrophys. J.* **370**, 130 (1991).
37. E. Hubble, *Astrophys. J.* **64**, 321 (1926).
38. A. V. Mosenkov, N. Ya. Sotnikova, and V. P. Reshetnikov, *Mon. Not. R. Astron. Soc.* **401**, 559 (2010).
39. S. Comerón, H. Salo, E. Laurikainen, J. H. Knapen, R. J. Buta, M. Herrera-Endoqui, J. Laine, B. W. Holwerda, K. Sheth, M. W. Regan, J. L. Hinz, J. C. Muñoz-Mateos, A. Gil de Paz, K. Menéndez-Delmestre, M. Seibert, et al., *Astron. Astrophys.* **562**, A121 (2014).
40. E. Laurikainen, H. Salo, E. Athanassoula, A. Bosma, R. Buta, and J. Janz, *Mon. Not. R. Astron. Soc.* **430**, 3489 (2013).

*Translated by D. Gabuzda*